International Journal of Applied Earth Observation and Geoinformation 151 (2026) 105399

Contents lists available at ScienceDirect

International Journal of Applied Earth Observation and Geoinformation

journal homepage: www.elsevier.com/locate/jag

The role of atmospheric correction errors in the underestimation of satellite-derived chlorophyll-*a* concentration in the Southern Ocean

Tianhao Wang [a], Zhongping Lee [a,b], David Antoine [c,d], Longteng Zhao [a], Xu Li [a], Lingling Li [a], Yalong Zhang [a], Daosheng Wang [a], Shaoling Shang [a,b], Gong Lin [a], Xiaolong Yu [a,*]

[a] State Key Laboratory of Marine Environmental Science, College of Ocean and Earth Sciences, Xiamen University, Xiamen 361102, China
[b] Fujian Ocean Innovation Center, Xiamen 361102, China
[c] Remote Sensing and Satellite Research Group, School of Earth and Planetary Sciences, Curtin University, Perth, WA 6845, Australia
[d] ARC Australian Centre for Excellence in Antarctic Science (ACEAS), University of Tasmania, Hobart, TAS 7001, Australia

A R T I C L E I N F O

Keywords:
Remote sensing reflectance
Cross-Satellite Atmospheric Correction
Chlorophyll-*a* concentration
VIIRS
Southern Ocean

A B S T R A C T

Previous studies have consistently reported underestimation of satellite-derived chlorophyll-*a* concentration (CHL) in the Southern Ocean (SO). While this bias is often attributed to the region's unique bio-optical properties, the potential contribution of atmospheric correction errors has been comparatively underexplored. This study evaluated the performance of three mainstream CHL retrieval algorithms (OC2, OC3, OCI) in high-latitude waters of the SO, mainly poleward of 63°S, using three types of remote-sensing reflectance (R_{rs}) data: in-situ R_{rs}, NASA-distributed standard VIIRS R_{rs}, and VIIRS R_{rs} obtained from a recently developed Cross-Satellite Atmospheric Correction (CSAC) algorithm. Our results show that when in-situ R_{rs} were used as inputs, the mean absolute percent difference (MAPD) values between measured and estimated CHL by OC2, OC3, and OCI were 24.4%, 23.0%, and 30.2%, respectively. Using NASA-distributed VIIRS R_{rs} increased the MAPD values to 41.7%, 50.4%, and 55.4%, respectively. In contrast, when CSAC-derived R_{rs} were used, the MAPD values reduced to 25.4%, 22.5%, and 21.4%, respectively. This is because CSAC-derived R_{rs} showed much stronger agreement with in-situ R_{rs} than NASA-distributed R_{rs}, with MAPD values reduced by approximately 50% across the visible bands. These results suggest that imperfect atmospheric correction plays a big role in the systematic underestimation of CHL in the SO from ocean color remote sensing. Additionally, CSAC was able to recover CHL retrievals under challenging observation conditions, such as moderate sunglint and straylight, which were previously masked in the standard VIIRS product, thereby substantially improving data coverage. Therefore, we anticipate that incorporating CSAC into the production of ocean color products will yield more accurate, better spatially covered products in this critical region.

1. Introduction

The Southern Ocean (SO), encircling Antarctica, plays a crucial role in regulating Earth's climate, driving deep ocean circulation, and supporting diverse marine ecosystems (Gray, 2024; Mayewski et al., 2009; Morley et al., 2020; Murphy et al., 2021). Accounting for a significant portion of global carbon uptake, the SO acts as a major sink for atmospheric CO_2, exchanging vast amounts of heat and nutrients between the equator and the poles (Frölicher et al., 2015; Long et al., 2021; Williams et al., 2023). It is therefore essential to accurately monitor the dynamics of phytoplankton and the associated biogeochemical processes in this region. Due to its remoteness and harsh environmental conditions, satellite ocean color remote sensing has become an indispensable tool for monitoring its ocean color parameters (Del Castillo et al., 2019; Moore et al., 1999; Thomalla et al., 2023).

However, Marrari et al. (2006) showed that satellite-derived chlorophyll-*a* concentration (CHL) was underestimated by up to 50% compared to in-situ measurements. This was echoed by Johnson et al. (2013) and Moutier et al. (2019), and further highlighted by Chen et al. (2021). Such biases may also weaken the observed intensity of phytoplankton blooms from satellite CHL products (D'Sa et al., 2021; Salyuk et al., 2025). These studies all used CHL products derived from

* Corresponding author at: State Key Laboratory of Marine Environmental Science, College of Ocean and Earth Sciences, Xiamen University, Xiamen 361102, China.

E-mail address: xlyu@xmu.edu.cn (X. Yu).

https://doi.org/10.1016/j.jag.2026.105399
Received 4 March 2026; Received in revised form 3 June 2026; Accepted 4 June 2026
Available online 8 June 2026

band-ratio algorithms. No similar systematic large underestimation was observed by Haëntjens et al. (2017), who compared MODIS satellite CHL derived from the band-difference algorithm of Hu et al. (2012) and in-situ CHL derived from fluorescence measurements on Biogeochemical-Argo floats.

To address this issue, researchers have developed regionally tuned CHL algorithms tailored to SO conditions (Garcia et al., 2005; Jena, 2017; Marrari et al., 2006). For instance, Chen et al. (2021) recently developed regionally tuned algorithms for the Ross Sea by directly matching the remote sensing reflectance (R_{rs}) distributed by NASA with in-situ CHL and particulate organic carbon (POC) measurements. A similar approach was used at the scale of the entire Southern Ocean by Cha et al. (2025). However, such efforts do not explicitly resolve how much of the persistent CHL underestimation arises from inadequacies in global CHL algorithms adopted by space agencies or from the quality of R_{rs} inputs used in algorithm application.

Hypotheses have been proposed to explain this underestimation. One attributes it to the region's unique bio-optical properties, such as distinct particle size distributions (Allison et al., 2010; Kostadinov et al., 2009), pigment packaging effects (Jena, 2017; Robinson et al., 2021; Tripathy et al., 2014) or increased absorption by non-algal particles (Li et al., 2024), which might be very different from the assumptions underlying the CHL algorithms developed for the global ocean. Other authors point to the challenges of atmospheric correction (AC) in the SO, primarily due to high solar zenith angles (SOZA) (Li et al., 2022), frequent cloud cover (Haynes et al., 2011), high wind speeds that lead to whitecap contamination (Randolph et al., 2017; Scanlon and Ward, 2016), and complex aerosol conditions (Bigg, 1990; Li et al., 2022; Simmonds, 2003). These factors may increase uncertainties of satellite-derived R_{rs}, particularly in the blue-green spectral range on which CHL algorithms heavily rely. Despite this potential role of atmospheric correction on CHL retrievals in the SO, there has been a lack of relevant data or studies.

This study aims to examine this knowledge gap by leveraging recent field measurements of both R_{rs} and CHL in SO waters. Our analyses indicate that the imperfect atmospheric correction of the standard AC algorithm results in overestimation of R_{rs} in the blue, which subsequently leads to underestimation of CHL. However, CHL underestimation would be substantially mitigated when applying the Cross-Satellite Atmospheric Correction (CSAC) scheme (Lee et al., 2024), which yielded much better agreements between satellite and in-situ measurements for both R_{rs} and CHL in this study. This study thus offers insight into the causes of CHL underestimation reported in the literature and demonstrates the benefit of using the CSAC algorithm for ocean color remote sensing in polar regions.

2. Data and methods

2.1. In-situ measurements

Field measurements of both R_{rs} and CHL collected in the SO during the 38th Chinese National Antarctic Research Expedition aboard the R/V Xuelong icebreaker were used in this effort. In total, we collected 121 in-situ R_{rs} measurements during this expedition from December 2nd, 2021 to March 8th, 2022, with Fig. 1 showing the sampling locations. The samples were collected from high-latitude and nearshore waters, mainly poleward of 63°S, surrounding the Antarctic continent, encompassing environments from relatively clear to highly optically complex conditions (Zhang et al., 2024).

The radiometric measurements were acquired using a GER1500 spectroradiometer (Spectra Vista Corporation, USA), which covers a spectral range of 350–1050 nm with a spectral resolution of 3 nm. Following NASA ocean optics protocols, each complete measurement cycle comprised sequential acquisitions of the upwelling radiance above the water surface ($L_u(\lambda)$), the sky radiance at the reciprocal angle ($L_{sky}(\lambda)$), and the sky radiance reflected from a horizontal gray plaque

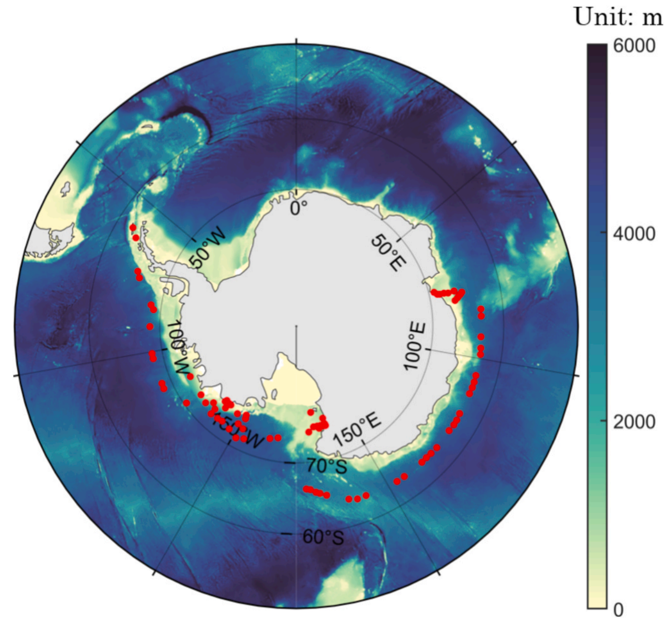

Fig. 1. Sampling locations of in-situ data in the SO (red dots), with the color bar representing bathymetry. (For interpretation of the references to colour in this figure legend, the reader is referred to the web version of this article.)

($L_{plaque}(\lambda)$). This cycle was repeated ten times at each sampling station. After filtering outliers, the remaining measurements were averaged and used to calculate R_{rs} as

$$R_{rs}(\lambda) = \rho \frac{\overline{L_u(\lambda)} - r\overline{L_{sky}(\lambda)}}{\pi \overline{L_{plaque}(\lambda)}} - \Delta, \quad (1)$$

where $\overline{L_u(\lambda)}$, $\overline{L_{sky}(\lambda)}$ and $\overline{L_{plaque}(\lambda)}$ denote the mean values of each radiance type across 10 repeated measurements. ρ (approximately 0.5) is the reflectance of the Spectralon® plaque, while both the air–water interface reflectance (r, fixed at 0.023) (Hooker and Morel, 2003; Lee et al., 2010; Mobley, 1999; Ruddick et al., 2000), and the residual surface reflectance (Δ, in units of sr^{-1}) were derived following the method described in Lee et al. (2010).

Note that only good-quality spectral R_{rs} were used for subsequent analyses, defined as those with a quality assurance score exceeding 0.5 (Wei et al., 2016). After quality control, a total of 92 stations with concurrent measurements of R_{rs} and CHL were retained. A detailed description of this Antarctic cruise is provided in Zhang et al. (2024).

In-situ CHL were measured using chlorophyll fluorescence methods (Holm-Hansen et al., 1965; Welschmeyer, 1994), based on water samples collected from the upper 5 m at each station. These near-surface CHL measurements ranged from 0.15 to 5.76 mg m^{-3}, with a median value of 0.97 mg m^{-3}. The dataset, therefore, covered a broad range of phytoplankton biomass conditions encountered along the cruise track, although very clear waters with CHL < 0.2 mg m^{-3} were relatively underrepresented.

2.2. Satellite data

Satellite observations from the Visible Infrared Imaging Radiometer Suite onboard the Suomi National Polar-orbiting Partnership weather satellite (VIIRS-SNPP) acquired from the NASA Ocean Color Web (https://oceandata.sci.gsfc.nasa.gov/) are used in this study. All valid VIIRS-SNPP measurements over the SO during the field campaign (*i.e.*, December 2nd, 2021 to March 8th, 2022) were acquired, resulting in a total of 2,078 VIIRS-SNPP images. These acquisitions provided broad spatial and temporal coverage across diverse environmental and observational conditions in the SO.

For VIIRS data, both the Level-1A (L1A) and Level-2 (L2) products were downloaded. The L1A products were then processed using SeaDAS v8.4.0 to generate top-of-atmosphere reflectance (ρ_t) and four viewing geometry parameters: SOZA, sensor zenith angle (SEZA), solar azimuth angle (SOAA), and sensor azimuth angle (SEAA). These data are key inputs for the CSAC scheme. During this processing step, quality control of satellite measurements was performed using the L2 Mask Default Flags (L2_FLAGS, https://oceancolor.gsfc.nasa.gov/resources/atbd/ocl2flags/). Pixels affected by land contamination, excessive radiance, stray light, clouds, and ice coverage were excluded from the analysis. The downloaded VIIRS L2 R_{rs} products were used to evaluate the performance of the "standard" AC algorithm in this region.

In addition, the ρ_t data of VIIRS were processed with the recently developed cross-satellite atmosphere correction (CSAC) algorithm (Lee et al., 2024), with a version specifically tuned for VIIRS-SNPP (termed $CSAC_{VIIRS}$). Generally, CSAC is a data-driven system that improves the consistency between R_{rs} of other ocean color satellites and that of MODIS-Aqua, with the highest quality R_{rs} product from MODIS-Aqua (HQMA-R_{rs}) used as the reference for model training. Details of the CSAC concept and demonstrations can be found in Lee et al. (2024). The inputs of $CSAC_{VIIRS}$ include ρ_t at ten VIIRS bands (*i.e.*, 410, 443, 486, 551, 671, 745, 862, 1238, 1601, and 2257 nm), four geometric angles (*i.e.*, SOZA, SEZA, SOAA, and SEAA), and three atmospheric parameters (ozone, water vapor, and sea surface pressure) from ERA5 (https://cds.climate.copernicus.eu/). The R_{rs} outputs of $CSAC_{VIIRS}$ are provided at the MODIS-Aqua bands (*i.e.*, 412, 443, 488, 531, 547, and 667 nm). It is important to clarify that the $CSAC_{VIIRS}$ training dataset, acquired throughout 2020, included a substantial proportion of samples representative of high-latitude (~15%) and high SOZA (~15%) conditions (Wang et al., 2026). The matchup dataset used in this study, compiled between December 2021 and March 2022, offers an entirely independent evaluation of $CSAC_{VIIRS}$ under high-latitude and high-SOZA conditions.

For satellite matchups, a spatial window of 3 × 3 km and a ± 24-hour temporal window were applied to match in-situ stations with satellite observations, resulting in 52 valid matchups with VIIRS observations. The 24-hour temporal window was used to retain a larger number of matchups for statistically robust analysis. In fact, the mean absolute difference in acquisition time of the obtained matchups was only 3.4 h, with only seven out of 52 matchups exceeding a 6-hour difference. Thus, using a narrower temporal window, such as 6 h, will not substantially affect the evaluation results.

2.3. CHL retrieval algorithms

We applied three commonly used "standard" algorithms, which include OC2 (O'Reilly et al., 1998), OC3 (O'Reilly et al., 2000), and the ocean color index (OCI) algorithm (Hu et al., 2012), to estimate CHL from VIIRS observations for the SO. OC2 and OC3, collectively referred to as OCx, are empirical algorithms that estimate CHL from the ratio of R_{rs} at selected blue and green wavelengths. These OCx algorithms are expressed as,

$$CHL_{OCx} = 10^{a0+a1\times R_{bgm}+a2\times R_{bgm}^2+a3\times R_{bgm}^3+a4\times R_{bgm}{}^4}. \tag{2}$$

Here, R_{bgm} is defined as $\log_{10}\frac{R_{rs}(\lambda_{blue})}{R_{rs}(\lambda_{green})}$, where $R_{rs}(\lambda_{blue})$ and $R_{rs}(\lambda_{green})$ refer to R_{rs} values at the blue and green bands. The coefficients *a0–a4* are sensor-specific empirical parameters. The main difference between OC2 and OC3 lies in their use of blue bands: OC2 employs the blue band near 490 nm solely, whereas OC3 uses the higher R_{rs} values between 440 and 490 nm.

For the in-situ R_{rs} collected during our SO cruise, most samples exhibited higher R_{rs} values at 440 nm than at 490 nm (Zhang et al., 2024). Therefore, comparing OC2 and OC3 helps reveal the sensitivity of CHL retrievals to uncertainties in R_{rs} at these two blue bands (440 and 490 nm). In this study, VIIRS-specific parameters (*a0–a4*) for OC2 and OC3 algorithms were used for both in-situ and standard VIIRS R_{rs} products, whereas MODIS-based parameters were used for $CSAC_{VIIRS}$ R_{rs} products (sensor-specific values of *a0–a4* provided in Table S1). A sensitivity test (not shown here) indicates that the use of different sensor-specific coefficients results in an overall difference of approximately 6–8% in the derived CHL values.

The OCI algorithm merges the OCx and a band-difference-based algorithm for CHL retrieval in oligotrophic waters (Hu et al., 2019; Hu et al., 2012), which is expressed as:

$$CI = R_{rs}(555) - \left[R_{rs}(443) + \frac{555-443}{670-443} \times (R_{rs}(670) - R_{rs}(443))\right],$$

$$CHL_{Hu} = 10^{-0.4909+191.6590\times CI},$$

$$CHL_{OCI} = \begin{cases} CHL_{Hu}\left[CHL_{Hu} \leqslant 0.25mg/m^{-3}\right] \\ CHL_{OC3}\left[CHL_{Hu} > 0.35mg/m^{-3}\right] \\ \alpha \times CHL_{OC3} + \beta \times CHL_{Hu}\left[0.25 < CHL_{Hu} \leqslant 0.35mg/m^{-3}\right] \end{cases}, \tag{3}$$

where *CI* is termed a color index, CHL_{Hu} is the CHL derived from *CI*, and $\alpha=(CHL_{Hu}-0.25)/0.1$, $\beta=(0.35-CHL_{Hu})/0.1$. Note that the threshold used here follows the updated parameterization for the generation of NASA standard CHL products (Hu et al., 2019), rather than the original values proposed in Hu et al. (2012). In addition, green band R_{rs} of VIIRS was converted to $R_{rs}(555)$ following Chen and Hu (2017).

2.4. Accuracy assessment metrics

In addition to the coefficient of determination (R^2) from linear regression, the Root Mean Squared Difference (RMSD), the Mean Absolute Percentage Difference (MAPD), bias, and the Mean Percentage Difference (MPD) were used to evaluate the differences between derived and "known" CHL or R_{rs}. These metrics are calculated as follows:

$$R^2 = 1 - \frac{\sum_{i=1}^{N}(Y_i - X_i)^2}{\sum_{i=1}^{N}(X_i - \overline{X})^2}, \tag{4}$$

$$RMSD = \sqrt{\frac{1}{N}\sum_{i=1}^{N}(Y_i - X_i)^2}, \tag{5}$$

$$MAPD = \frac{1}{N}\sum_{i=1}^{N}\left|\frac{Y_i - X_i}{X_i}\right| \times 100\%, \tag{6}$$

$$bias = \overline{Y} - \overline{X}, \tag{7}$$

$$MPD = \frac{1}{N}\sum_{i=1}^{N}\frac{Y_i - X_i}{X_i} \times 100\%, \tag{8}$$

where X_i and Y_i represent the reference and estimated quantities, and $\overline{X}$ and $\overline{Y}$ are their corresponding averages. N is the total number of samples. Here, X_i represents the reference CHL or R_{rs} values obtained from both the HQMA-R_{rs} products and the in-situ measurements.

3. Results and discussion

3.1. Performance of standard CHL algorithms using in-situ R_{rs}

We first assessed the performance of the three CHL algorithms using in-situ data. As shown in Fig. 2, when using in-situ R_{rs} as input, all three CHL algorithms demonstrate good performance in the SO, at least for the data used in this study. Specifically, the biases in the estimated CHL are close to zero, with values of –0.06 mg/m^3, –0.09 mg/m^3, and –0.1 mg/m^3 for OC2, OC3, and OCI, respectively. Correspondingly, the MAPD values range from 23% to 30.2%, and R^2 values exceed 0.70 for all algorithms. These results are consistent with performance reported for

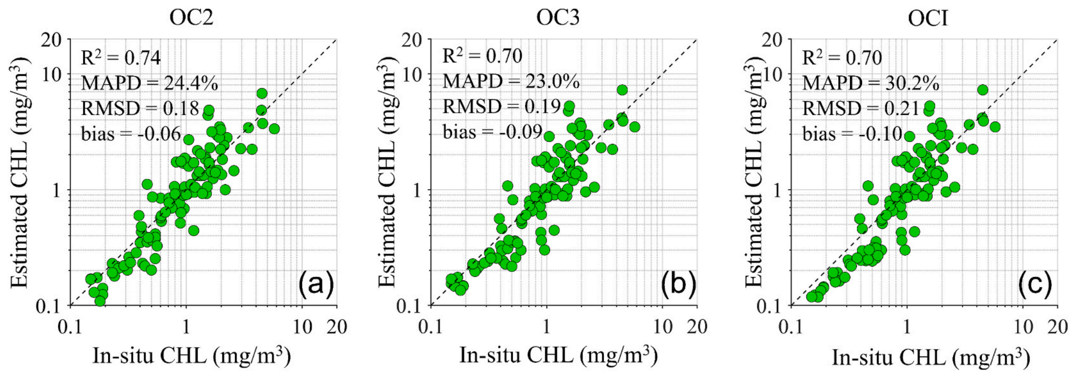

Fig. 2. Comparisons between in-situ CHL and estimates from different algorithms (OC2, OC3, and OCI) using in-situ R_{rs} as input (N = 92). The gray dashed line represents the 1:1 regression line. RMSD and bias are expressed in the same units as CHL (mg/m^3).

global datasets (Hu et al., 2019; O'Reilly and Werdell, 2019), indicating that these "standard" CHL algorithms, originally developed for the global ocean, perform reasonably well in the SO when provided with reliable R_{rs} inputs. These findings in general suggest that the commonly reported underestimation of CHL in the SO is unlikely to originate from algorithmic limitations. It is surprising that CHL_{Hu} tends to underestimate CHL at the lower concentration range (Fig. 2c), showing a mean bias of –0.10 mg/m^3 for the 24 samples with CHL_{Hu} < 0.25 mg/m^3. Further investigations into the robustness of the band-difference algorithm in oligotrophic waters of the SO may therefore be needed, though this is beyond the scope of the present study.

3.2. Evaluation of CHL retrieval algorithms using the VIIRS R_{rs} products

The performance of the three CHL algorithms was further evaluated using the standard VIIRS L2 R_{rs} as the input. As shown in the upper panel of Table 1, derived CHL from VIIRS L2 R_{rs} by all CHL algorithms exhibited more substantial uncertainties compared to retrievals from in-situ R_{rs}, with negative biases of –0.15, –0.25, and –0.28 mg/m^3 for OC2, OC3, and OCI, respectively (see Fig. 3a–3c). Furthermore, the MAPD values also increased sharply (see Fig. 3, particularly for OC3 and OCI), where the MAPD exceeded 50%. Since all algorithms perform reasonably well with in-situ R_{rs}, the underestimation of the VIIRS-derived CHL was likely related to the quality of the satellite-measured R_{rs}. We further examined the influence of the four outliers with the largest discrepancies in Fig. 3c, which are highlighted by green circles. After excluding these four points, the MAPD values for OC2, OC3, and OCI changed from 41.7%, 50.4%, and 55.4% to 34.8%, 43.2%, and 46.9%, respectively, while the negative biases remained evident at –0.06, –0.15, and –0.17 mg m^{-3}. This test indicates that the overall underestimation pattern is not solely driven by these few outliers.

In addition, according to Eq. (2), OC2 and OC3 follow the same algorithmic structure, with OC3 incorporating R_{rs}(443). Therefore, the more pronounced underestimation by OC3 likely stems from the stronger overestimation of R_{rs}(443) compared to R_{rs}(486)—a point that will be further examined in Section 3.4.1. It should be noted that the matchups with large SOZA were mostly located at higher latitudes and closer to the Antarctic shelf or sea-ice-influenced waters, where CHL is generally higher. Thus, the apparent association between large SOZA and high CHL mainly reflects the spatial distribution of the dataset rather than a causal relationship.

To investigate the potential influence of observational geometry on CHL retrievals, the in situ-satellite matchups were split between those with SOZA < 70°, where traditional AC algorithms generally perform well (Gordon and Wang, 1994; Wang, 2002), and those with SOZA ≥ 70°, where these algorithms often face challenges (He et al., 2018; Li et al., 2017). As shown in the upper two rows of Table 1, under large SOZA (≥70°) conditions, the biases (MPD) in estimated CHL reached –0.17 (–28.7%), –0.32 (–59.1%), and –0.33 mg/m^3 (–59.2%) for OC2, OC3, and OCI, respectively. This contrasts with the much smaller biases (MPD) values for observations under small SOZA (<70°), all within –0.24 mg/m^3 (–39.4%). Notably, the MAPD values under large SOZA exceeded 70% for all three algorithms, compared with 24.5–46.1% under small SOZA. These results further confirm that atmospheric correction errors, which are pronounced at large SOZA, play a major role in the substantial underestimation of CHL in the SO.

3.3. Performance of standard CHL algorithms using R_{rs} obtained by CSAC

The lower panel of Fig. 3 presents a comparison between in-situ CHL and that derived from $CSAC_{VIIRS}$ R_{rs} using the same three CHL algorithms, with corresponding statistical measures for two observational conditions reported in the lower two rows of Table 1. Compared with the results based on the NASA-distributed VIIRS R_{rs} products (Fig. 3a–3c),

Table 1
Statistical metrics for CHL derived from three retrieval algorithms (OC2, OC3, and OCI) using VIIRS and $CSAC_{VIIRS}$ R_{rs} as inputs, under both small and large SOZA conditions.

R_{rs} sources	SOZA range	Algorithms	bias (mg/m^{-3})	MAPD	MPD	RMSD (mg/m^{-3})	N
VIIRS	Small SOZA	OC2	−0.10	24.5%	−0.1%	0.30	32
		OC3	−0.21	38.7%	−32.0%	0.40	
		OCI	−0.24	46.1%	−39.4%	0.43	
VIIRS	Large SOZA	OC2	−0.17	72.8%	−28.7%	0.88	20
		OC3	−0.32	70.3%	−59.1%	0.98	
		OCI	−0.33	71.3%	−59.2%	0.99	
$CSAC_{VIIRS}$	Small SOZA	OC2	0.03	22.6%	13.2%	0.17	32
		OC3	0.02	16.6%	2.2%	0.19	
		OCI	−0.03	14.7%	2.0%	0.19	
$CSAC_{VIIRS}$	Large SOZA	OC2	−0.06	30.1%	−11.0%	0.43	20
		OC3	−0.15	32.1%	−18.9%	0.50	
		OCI	−0.15	32.2%	−18.9%	0.50	

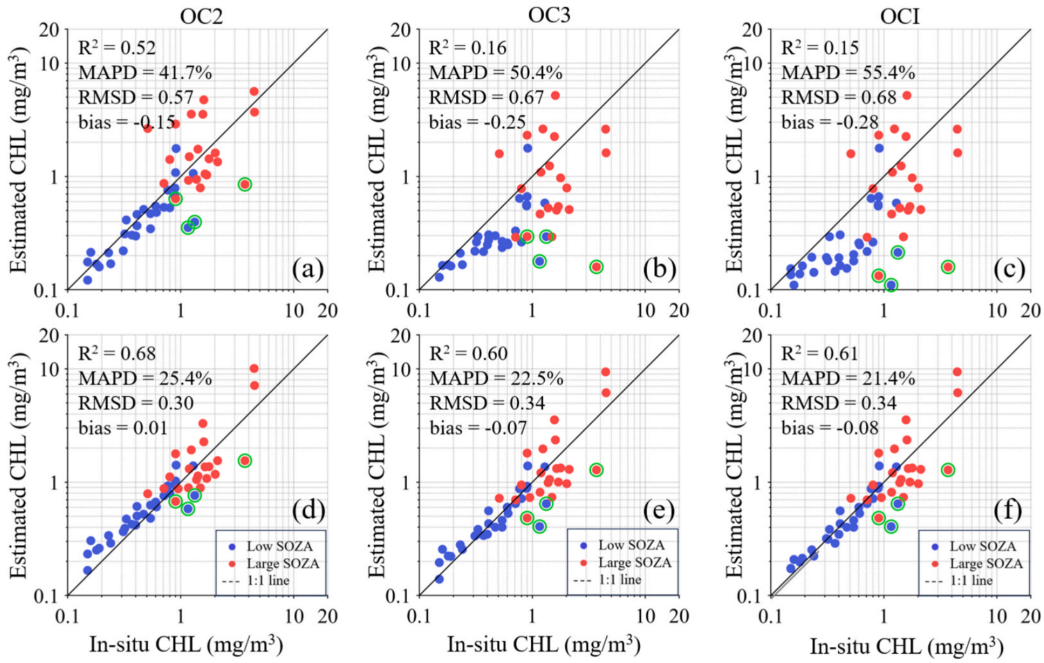

Fig. 3. Comparisons between in-situ CHL and estimates from different algorithms (OC2, OC3, and OCI) using various R_{rs} inputs. The upper and lower panels are for the evaluations of VIIRS standard L2 R_{rs} and CSAC$_{\mathrm{VIIRS}}$ R_{rs} (N = 52), respectively. Satellite measurements acquired under small (<70°, N = 32) and large SOZA (≥70°, N = 20) are distinguished with blue and red dots, respectively. The gray dashed line represents the 1:1 regression line. RMSD and bias are expressed in the same units as CHL (mg/m^3). The four stations with the largest discrepancies in panel (c) are highlighted with green circles. (For interpretation of the references to colour in this figure legend, the reader is referred to the web version of this article.)

CHL retrievals from CSAC$_{\mathrm{VIIRS}}$ R_{rs} show clear and substantial improvements. Biases across all algorithms are markedly reduced, shifting from pronounced underestimation (–0.15 to –0.28 mg/m^3) to near-zero values (see Fig. 3). For the four outliers, the biases are also reduced by more than half. The MAPD values also declined significantly from 41.7 to 55.4% for VIIRS L2 R_{rs} to 21.4–25.4% for CSAC$_{\mathrm{VIIRS}}$ R_{rs}. Notably, OCI exhibited the greatest improvement, achieving the lowest MAPD of 21.4%. These statistics demonstrate that using CSAC$_{\mathrm{VIIRS}}$ R_{rs} not only alleviates the systematic underestimation but also improves the overall retrieval accuracy with the "standard" CHL algorithms.

Moreover, using CSAC$_{\mathrm{VIIRS}}$ R_{rs} could significantly improve CHL retrieval under both small and large SOZA conditions (see Table 1). For instance, under large SOZA conditions, where the standard VIIRS R_{rs} resulted in substantial CHL underestimation (bias around –0.3 mg/m^3, see Table 1), CHL derived from CSAC$_{\mathrm{VIIRS}}$ R_{rs} exhibited nearly negligible biases (–0.06, –0.15, and –0.15 mg/m^3 for OC2, OC3, and OCI, respectively). This marks a major improvement in CHL retrieval from satellite ocean color measurements in the SO.

Although the CSAC$_{\mathrm{VIIRS}}$ R_{rs} products greatly improve CHL retrieval in general, the MAPD values under large SOZA remain noticeably higher than those under small SOZA (see Table 1). This might be partly due to the much smaller sample numbers; it may also reflect the inherent challenge of accurately retrieving water-leaving radiance and R_{rs} under such conditions, when the radiance is very low. Nevertheless, these results reaffirm that providing higher-quality satellite R_{rs} inputs can lead to more reliable and consistent CHL products.

3.4. Evaluation of various VIIRS R_{rs} products in the Southern Ocean

3.4.1. Evaluation of the standard VIIRS L2 R_{rs}

The above analyses showed that the standard CHL retrieval algorithm performed significantly better when using in-situ or CSAC$_{\mathrm{VIIRS}}$ R_{rs} compared to the NASA-distributed VIIRS R_{rs}; thus, it is necessary to evaluate these R_{rs} products retrieved from VIIRS. We first compared the NASA-distributed L2 R_{rs} with matched in-situ R_{rs} across the five VIIRS visible bands and the blue-to-green band ratio, as shown in Fig. 4a–4f. The corresponding statistical metrics are tabulated in the upper section of Table 2.

As shown in Fig. 4a–4e, systematic overestimations of VIIRS R_{rs} are found for all five bands, with the bias most pronounced in the blue bands, reaching 0.0026 sr^{-1} at 410 nm, 0.0018 sr^{-1} at 443 nm, and 0.0013 sr^{-1} at 486 nm, respectively. Even for the green (551 nm) and red (671 nm) bands, where R_{rs} values are inherently lower, small yet consistent positive biases remain evident (0.0004 and 0.0002 sr^{-1}, respectively). Moreover, MAPD values exceed 69% at 410 nm and 64% at 443 nm, reflecting significant deviations of satellite R_{rs} from in-situ data. The absolute differences are also remarkable, as indicated by RMSD values, particularly at 410 nm (RMSD = 0.0064 sr^{-1}). And, the overestimation at $R_{rs}(443)$ in the standard VIIRS product is more pronounced than at $R_{rs}(490)$, leading to a larger discrepancy in CHL estimates between the OC3 and OC2 algorithms. Moreover, the strong dependence of OCI on $R_{rs}(443)$ also explains its poorer performance with the biased VIIRS L2 R_{rs}. Note that the errors in VIIRS L2 R_{rs} gradually decrease with increasing wavelength, except at 671 nm, where the MAPD remains above 80%, likely due to the very low R_{rs} values at this band. In addition, the R_{rs} band ratio $R_{rs}(443)/R_{rs}(551)$—widely used in empirical CHL algorithms (Gordon and Morel, 1983; Morel and Prieur, 1977; O'Reilly et al., 1998)—exhibits notable positive bias (0.33, see Fig. 4a and Table 2). Since the OCx algorithms generally express CHL as a nonlinear inverse function of this R_{rs} ratio, positive biases in the ratio will result in underestimated CHL.

Further analysis indicated that observation geometry is a key factor driving these discrepancies. We calculated the spectral biases of satellite R_{rs} products, termed $\Delta R_{rs}(\lambda)$, defined as the spectral difference between satellite-measured and matched in-situ-measured R_{rs}. The median $\Delta R_{rs}(\lambda)$ for VIIRS L2 R_{rs} is shown in Fig. 5a, highlighting that the overestimation of VIIRS R_{rs} is substantially amplified under large SOZA (≥ 70°), particularly in the blue bands. For instance, at 410 nm, ΔR_{rs} approaches 0.004 sr^{-1} under large SOZA conditions, approximately four times higher than that under small SOZA. This systematic

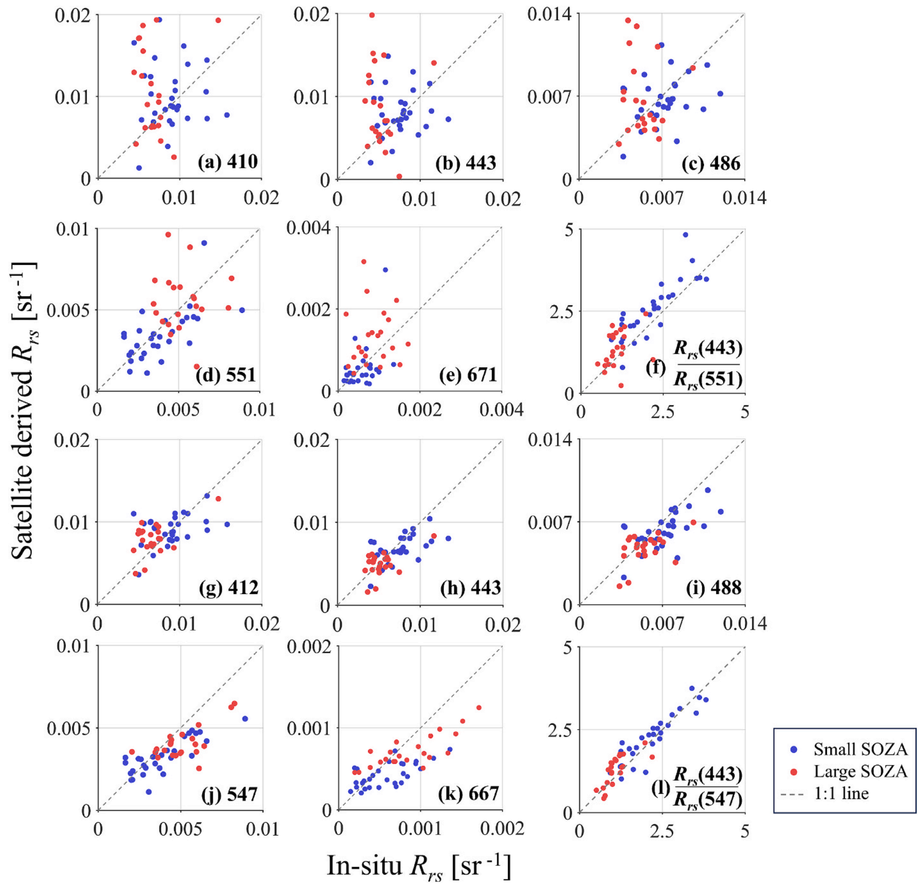

Fig. 4. Evaluation of VIIRS standard L2 R_{rs} products against matched in-situ R_{rs} at VIIRS visible bands (a–e) and the blue-to-green R_{rs} band ratio (f, dimensionless). Panels (g–l) show the corresponding evaluations for R_{rs} products from CSAC$_{VIIRS}$ at MODIS bands. (For interpretation of the references to colour in this figure legend, the reader is referred to the web version of this article.)

Table 2
Statistical metrics for evaluation results in Fig. 4 (N = 52).

VIIRS R_{rs} vs. in-situ R_{rs}					
Products	R^2	MAPD	MPD	RMSD (sr^{-1})	bias (sr^{-1})
R_{rs}(410)	0.07	69.70%	32.60%	0.0064	0.0026
R_{rs}(443)	0.03	64.80%	27.50%	0.0048	0.0018
R_{rs}(486)	0.05	41.40%	20.10%	0.0033	0.0013
R_{rs}(551)	0.26	46.80%	9.20%	0.0027	0.0004
R_{rs}(671)	0.36	82.60%	28.30%	0.0006	0.0002
R_{rs}(443)/R_{rs}(551)	0.75	35.50%	19.30%	0.44	0.33
CSAC$_{VIIRS}$ R_{rs} vs. in-situ R_{rs}					
Products	R^2	MAPD	MPD	RMSD (sr^{-1})	bias (sr^{-1})
R_{rs}(412)	0.49	35.20%	8.80%	0.003	0.0007
R_{rs}(443)	0.55	29.50%	−9.20%	0.0023	−0.0006
R_{rs}(488)	0.56	27.20%	15.30%	0.002	0.001
R_{rs}(547)	0.68	23.30%	2.30%	0.0012	−0.0001
R_{rs}(667)	0.5	47.30%	−28.30%	0.0003	−0.0002
R_{rs}(443)/R_{rs}(547)	0.85	18.90%	15.20%	0.26	0.08

overestimation across all visible bands, particularly in the blue and green bands that are critical for CHL retrievals, offers a plausible explanation for the pronounced underestimation of CHL presented in Section 3.2. Overall, these results further reinforce that the NASA standard atmospheric correction algorithm is inadequate for processing satellite ocean color observations under large SOZA (IOCCG, 2015; Li et al., 2022). Persistent large SOZA conditions, along with complex atmospheric properties, result in positively biased R_{rs} across the visible spectrum in the SO. Thus, the systematic overestimations of the satellite

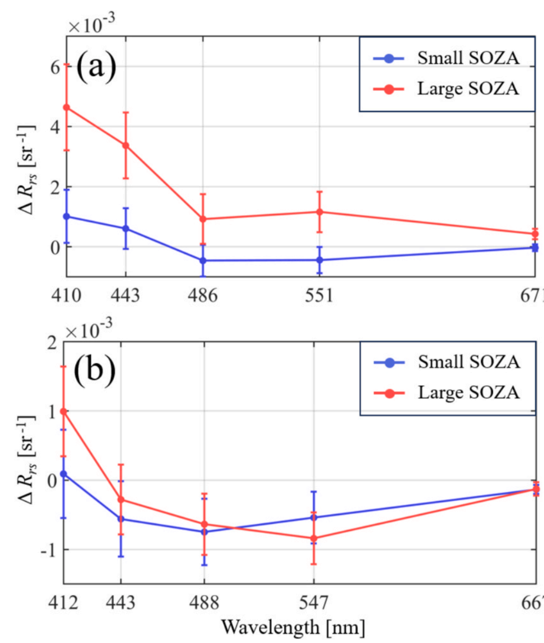

Fig. 5. Spectral biases (ΔR_{rs}) of (a) VIIRS L2 R_{rs} and (b) CSAC$_{VIIRS}$ R_{rs} relative to in-situ measurements under small (<70°) and large (≥70°) SOZA conditions, shown as mean ± standard deviation. Positive (negative) biases indicate systematic overestimation (underestimation) in different R_{rs} products.

standard R_{rs} propagate through CHL retrieval algorithms and contribute to the well-documented underestimation of CHL products in this region (Chen et al., 2021; Jena, 2017; Johnson et al., 2013).

3.4.2. $CSAC_{VIIRS}$ R_{rs} compared with in-situ measurements

Following the above practices, we evaluated the $CSAC_{VIIRS}$ R_{rs} against in-situ measurements, with results presented in Fig. 4g–4 l. Compared to the VIIRS L2 R_{rs} products shown in the upper two panels in Fig. 4, $CSAC_{VIIRS}$ R_{rs} exhibit pronounced and consistent improvements, markedly reducing the systematic overestimation observed in the VIIRS L2 R_{rs}. For instance, at 443 nm, the bias decreases from 0.0018 sr^{-1} (Fig. 4b) to just −0.0006 sr^{-1} (Fig. 4h). Comparable improvements are also observed across other bands, with biases in the $CSAC_{VIIRS}$ R_{rs} consistently below 0.001 sr^{-1} (Fig. 4g–k). Moreover, $CSAC_{VIIRS}$ also improves the estimation of $R_{rs}(443)/R_{rs}(547)$, reducing the bias from 0.33 to 0.08, and lowering the MAPD from 35.5% to 18.9% (see Table 2). These results suggest that the $CSAC_{VIIRS}$ not only corrects absolute reflectance values but also preserves the spectral relationships, thereby offering greater potential for producing more accurate CHL estimates.

We also calculated the spectral biases of $CSAC_{VIIRS}$ R_{rs} relative to in-situ R_{rs}, with the median $\Delta R_{rs}(\lambda)$ shown in Fig. 5b. Overall, $\Delta R_{rs}(\lambda)$ of $CSAC_{VIIRS}$ R_{rs} shows moderate improvement over VIIRS L2 R_{rs} for observations with small SOZA ($< 70^\circ$) (Fig. 5). However, for observations with SOZA $\geq 70^\circ$, remarkable improvements were observed in $CSAC_{VIIRS}$ R_{rs}. For instance, $\Delta R_{rs}(\lambda)$ for $CSAC_{VIIRS}$ R_{rs} generally remain close to zero (Fig. 5b), compared with biases as high as $\sim$ 0.005 sr^{-1} at 412 nm for the VIIRS L2 R_{rs} (Fig. 5a). These results further demonstrate that, compared to the conventional atmospheric correction algorithm, the $CSAC_{VIIRS}$ algorithm can deliver significantly better R_{rs} products for acquisitions under high SOZA conditions.

3.5. Difference in data coverage among various CHL maps

Previous evaluations have demonstrated that $CSAC_{VIIRS}$ R_{rs} can improve the accuracy and consistency of satellite-derived CHL in the SO. We then applied the $CSAC_{VIIRS}$ algorithm to VIIRS measurements to generate L2 and Level-3 composited (L3) CHL maps. Here, the L2 VIIRS image acquired at 00:54:00 UTC on December 28, 2021, was used as an example, with the resulting CHL maps from different R_{rs} inputs shown in Fig. 6.

As shown in Fig. 6, $CSAC_{VIIRS}$ R_{rs} yields a substantially higher number of valid pixels than VIIRS L2 R_{rs}. For example, most pixels within the red box in Fig. 6 are flagged as invalid in the VIIRS L2 product, primarily due to the influence of clouds and the potential cloud adjacency effect (see Fig. 6d). In contrast, $CSAC_{VIIRS}$ successfully restores CHL information, preserving features that would otherwise be lost. For this specific VIIRS image, $CSAC_{VIIRS}$ R_{rs} could recover up to 71.7% more valid CHL observations than VIIRS L2 R_{rs}. In addition, $CSAC_{VIIRS}$ R_{rs} produces on average 12.6% higher CHL estimates than the VIIRS L2 product (Fig. 6c), which are consistent with the results presented in earlier analyses using satellite-in-situ matchups. It was worth noting that only a few valid observations in this image are acquired under SOZA $\geq 70^\circ$, and therefore, the improvements in CHL values from $CSAC_{VIIRS}$ R_{rs} are relatively modest ($\sim$12.6%).

To further assess the impact of R_{rs} quality on CHL products in the SO, we compared Level-3 daily composited CHL maps derived from the standard VIIRS product (downloaded directly from the NASA Ocean-Color Web) with those derived using $CSAC_{VIIRS}$ R_{rs}. The L3 CHL mapping

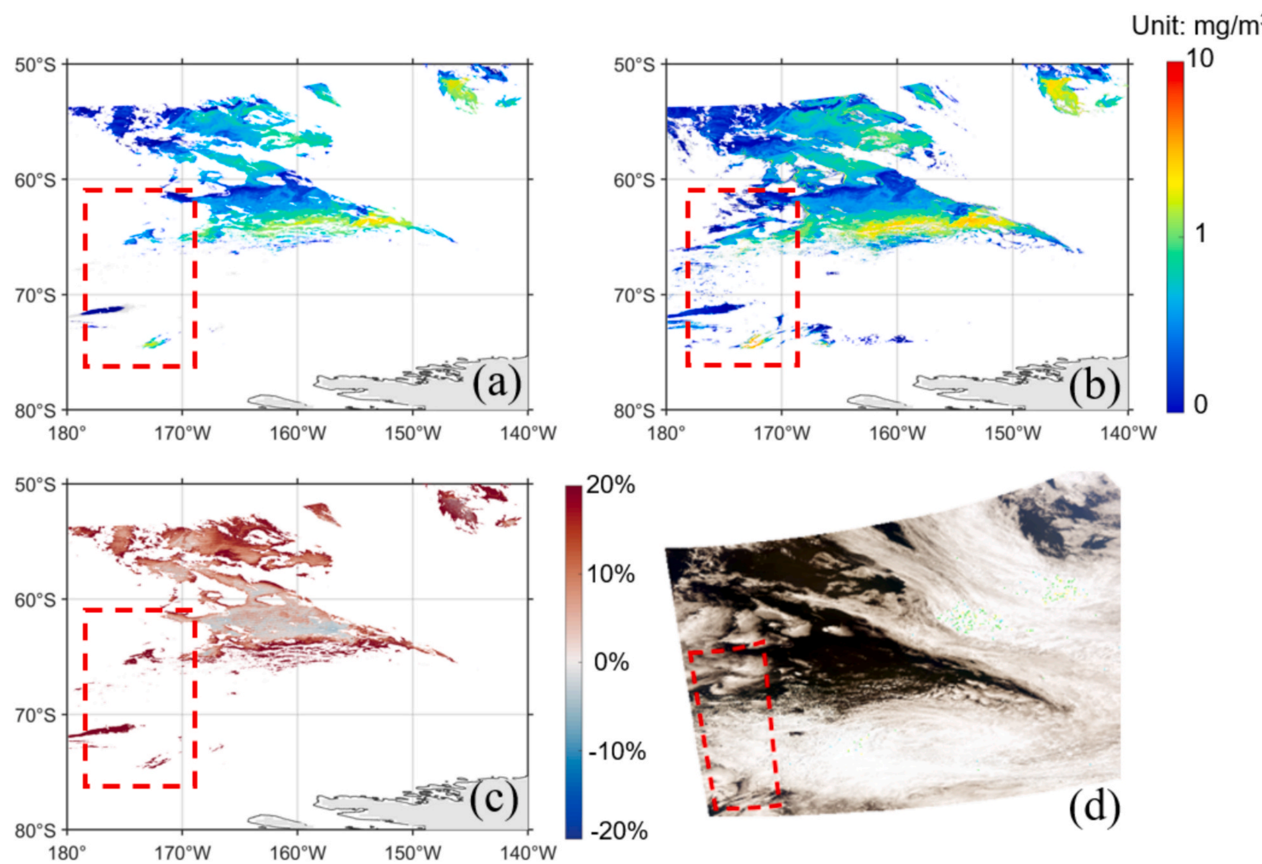

Fig. 6. The CHL mapping products derived from (a) standard VIIRS L2 and (b) $CSAC_{VIIRS}$ R_{rs} using the OCI algorithm for the image acquired at 00:54:00 UTC on December 28, 2021. Panel (c) shows the relative percentage difference between (b) and (a). Panel (d) shows the corresponding true-color composite imagery (from ρ_t at 443, 551, 671 nm) for reference. The red dashed rectangle marks a region in the Pacific sector of the Southern Ocean (168–178°W, 61–75°S). (For interpretation of the references to colour in this figure legend, the reader is referred to the web version of this article.)

product was generated by first compositing the L3 R_{rs} product and then applying the CHL algorithm (Fig. 7b). The L3 CHL product composited from the VIIRS L2 R_{rs} shows noticeable spatial discontinuities and limited data coverage (Fig. 7a), particularly near the Antarctic Circumpolar Current and coastal Antarctica, where hydrological conditions are more complex. In contrast, the $CSAC_{VIIRS}$-based CHL map (Fig. 7b) exhibits substantial improvements in both spatial coherence and data coverage, revealing fine-scale oceanographic features—such as frontal structures and high loads of phytoplankton—that are masked out in Fig. 7a.

We further examine L2_FLAGS of those recovered pixels by $CSAC_{VIIRS}$ to investigate the potential reasons why they were masked out in the standard Level-2 product. Specifically, 16.7% of those recovered pixels were flagged as affected by strong sunglint, while 22.1% and 9.4% were associated with large sensor and solar zenith angles, respectively. Among all factors, stray light contamination contributed the most to invalid observations, accounting for 51.8% of all masked pixels. This is unsurprising, considering the persistent cloud cover and complex atmospheric conditions in the SO, which amplify stray light effects in satellite observations. Unlike traditional atmospheric correction schemes, which often failed under such conditions, the CSAC framework maintains robust performance even in these challenging observational conditions.

In addition to the improved spatial coverage, Fig. 7c shows that CHL derived from $CSAC_{VIIRS}$ R_{rs} increases the median CHL value by 30.3% relative to the standard VIIRS product. This finding is consistent with the evaluations using in-situ-satellite matchups (Fig. 3), thereby substantially alleviating the long-standing CHL underestimation in the standard products. Overall, these results provide compelling evidence that $CSAC_{VIIRS}$ can substantially improve the spatial coverage and accuracy of VIIRS R_{rs} products, and the subsequent R_{rs}-derived products such as CHL. This improvement is particularly important for L2 and L3 products in the SO under challenging observational conditions where traditional atmospheric correction methods often fail. Given that $CSAC_{VIIRS}$ provides more accurate R_{rs} and CHL in the SO than standard VIIRS L2 products (Fig. 2 to Fig. 5), we can conclude with confidence that implementing CSAC could greatly enhance both the quality and quantity of ocean color data in the SO.

4. Conclusion

This paper investigates the underestimation of satellite-derived CHL in the SO, with a focus on the role of atmospheric correction errors using field measurements collected during a recent Antarctic cruise. Using field measurements of R_{rs} and CHL from a recent cruise, we found that biases in satellite-derived R_{rs} lead to inaccurate CHL retrievals. Specifically, the standard VIIRS R_{rs} products exhibit substantial overestimations in the blue bands, resulting in an underestimation of CHL. In contrast, applying the same CHL algorithms to in-situ R_{rs} or $CSAC_{VIIRS}$ R_{rs} effectively reduces this underestimation. This improvement is primarily attributed to the fact that CSAC can substantially reduce R_{rs} biases relative to in-situ measurements and enhance consistency with the highest quality MODIS-Aqua measurement, particularly under high SOZA conditions. Moreover, CSAC substantially enhances the data coverage of VIIRS observations in the SO, recovering over 70% more pixels that were previously masked due to moderate sunglint, stray light, and other factors.

Our results offer new insights into the long-standing underestimation of satellite-measured CHL in the SO, underscoring the critical role of accurate atmospheric correction in ensuring reliable bio-optical property retrievals. More importantly, these results demonstrate the effectiveness of the newly developed CSAC scheme in producing accurate and consistent ocean color products from satellite ocean color observations. We anticipate that applying CSAC to other satellite ocean color measurements in the SO will not only reduce biases but also greatly improve spatial coverage, thereby providing stronger support for oceanographic

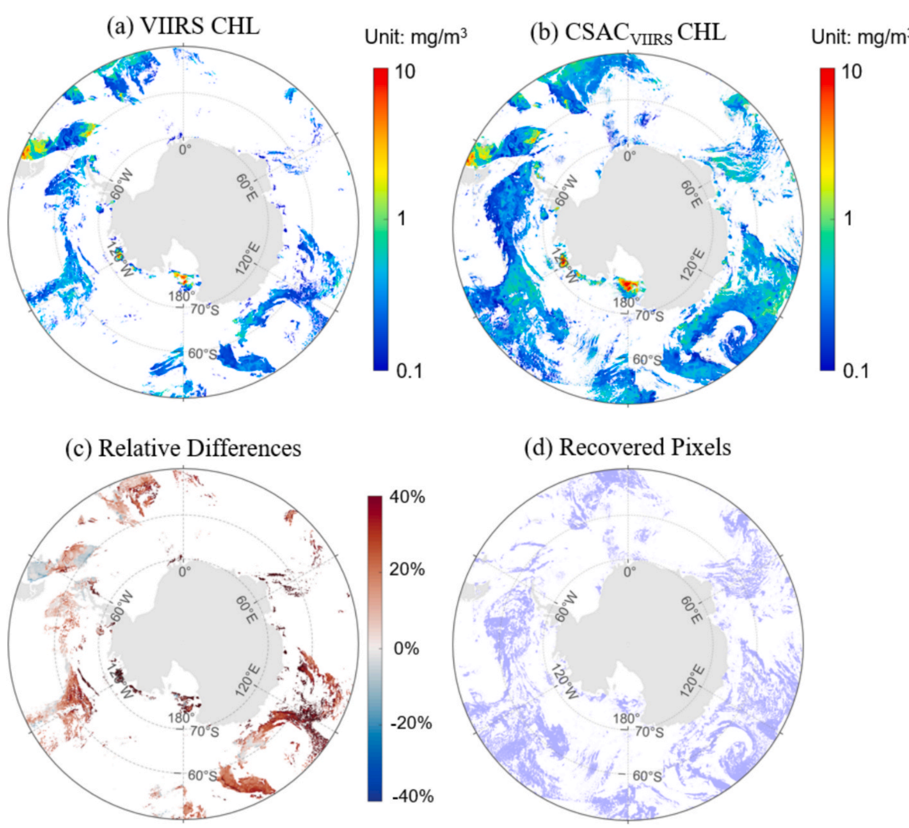

Fig. 7. Daily composite Level-3 CHL maps over the SO on December 2nd, 2020, from (a) standard VIIRS L3 product and (b) derived using the OCI algorithm from $CSAC_{VIIRS}$ R_{rs}. Panel (c) shows the relative percentage difference between (b) and (a). Panel (d) highlights the additional valid pixels recovered by $CSAC_{VIIRS}$.

studies in this ocean.

It must be acknowledged, however, that the in-situ measurements used in this study were collected during a single Antarctic expedition and therefore do not fully capture the interannual variability of atmospheric, bio-optical, and phytoplankton conditions in the SO. In addition, about 40% of the Southern Ocean has surface chlorophyll concentrations lower than 0.2 mg m^{-3} (Holm-Hansen et al., 2004; Marrari et al., 2006; Song and Ke, 2015). This significant body of clear waters is not well represented in our dataset, and further investigations about the performance of satellite algorithms and products in these waters may still be required. Future efforts should evaluate the performance of $CSAC_{VIIRS}$ using broader in-situ measurements in the SO spanning different seasons, regions, and trophic states. This evaluation could be necessary to build confidence in the capability of $CSAC_{VIIRS}$ to generate high-quality long-term satellite CHL products in the entire SO.

CRediT authorship contribution statement

Tianhao Wang: Writing – review & editing, Writing – original draft, Visualization, Validation, Supervision, Software, Resources, Project administration, Methodology, Investigation, Funding acquisition, Formal analysis, Data curation, Conceptualization. **Zhongping Lee:** Writing – review & editing, Conceptualization. **David Antoine:** Writing – review & editing, Data curation. **Longteng Zhao:** Software, Data curation. **Xu Li:** Software, Data curation. **Lingling Li:** Writing – review & editing. **Yalong Zhang:** Software, Data curation. **Daosheng Wang:** Software. **Shaoling Shang:** Writing – review & editing. **Gong Lin:** Data curation. **Xiaolong Yu:** Writing – review & editing, Writing – original draft, Conceptualization.

Declaration of competing interest

The authors declare that they have no known competing financial interests or personal relationships that could have appeared to influence the work reported in this paper.

Acknowledgments

This work was supported by the National Key Research and Development Program of China (2024YFF0808900), the National Natural Science Foundation of China (42430107 and 42376173), the National Key Research and Development Program of China (2022YFC3104900), the Fundamental Research Funds for the Central Universities (20720240102), and the MEL Internal Program (MELRI2602 and MELRI2605). We thank Ms. Ying Su for her assistance during the execution of the above projects. Support from all the cruise members of the 38th Chinese National Antarctic Research Expedition is greatly appreciated, which made the collection of bio-optical properties in the Southern Ocean possible. A portion of the data and samples was collected during the open research cruises NORC2023-11, NORC2025-02, NORC2024-04, supported by NSFC Shiptime Sharing Project (project numbers: 42249911, 42449902, 42349904).

Appendix A. Supplementary data

Supplementary data to this article can be found online at https://doi.org/10.1016/j.jag.2026.105399.

Data availability

Data will be made available on request.

References

Allison, D.B., Stramski, D., Mitchell, B.G., 2010. Seasonal and interannual variability of particulate organic carbon within the Southern Ocean from satellite ocean color observations. J. Geophys. Res. Oceans, 115.

Bigg, E., 1990. Aerosol over the southern ocean. Atmos. Res. 25, 583–600.

Cha, M., Pang, X., Antoine, D., 2025. Development of Parameter-Tuned Algorithms for Chlorophyll-a Concentration estimates in the Southern Ocean. Remote Sens. (Basel) 17, 3595.

Chen, S., Hu, C., 2017. Estimating sea surface salinity in the northern Gulf of Mexico from satellite ocean color measurements. Remote Sens. Environ. 201, 115–132.

Chen, S., Smith Jr, W.O., Yu, X., 2021. Revisiting the Ocean Color Algorithms for Particulate Organic Carbon and Chlorophyll-a Concentrations in the Ross Sea. J. Geophys. Res. Oceans 126, e2021JC017749.

D'Sa, E.J., Kim, H.-C., Ha, S.-Y., Joshi, I., 2021. Ross Sea dissolved organic matter optical properties during an Austral summer: Biophysical influences. Front. Mar. Sci. 8, 749096.

Del Castillo, C.E., Signorini, S.R., Karaköylü, E.M., Rivero-Calle, S., 2019. Is the Southern Ocean getting greener? Geophys. Res. Lett. 46, 6034–6040.

Frölicher, T.L., Sarmiento, J.L., Paynter, D.J., Dunne, J.P., Krasting, J.P., Winton, M., 2015. Dominance of the Southern Ocean in anthropogenic carbon and heat uptake in CMIP5 models. J. Clim. 28, 862–886.

Garcia, C.A.E., Garcia, V.M.T., McClain, C.R., 2005. Evaluation of SeaWiFS chlorophyll algorithms in the Southwestern Atlantic and Southern Oceans. Remote Sens. Environ. 95, 125–137.

Gordon, H.R., Morel, A.Y., 1983. In—water algorithms. *Remote assessment of ocean color for interpretation of satellite visible imagery: a review*. Springer, pp. 24–67.

Gordon, H.R., Wang, M., 1994. Retrieval of water-leaving radiance and aerosol optical thickness over the oceans with SeaWiFS: a preliminary algorithm. Appl. Opt. 33, 443–452.

Gray, A.R., 2024. The four-dimensional carbon cycle of the Southern Ocean. Ann. Rev. Mar. Sci. 16, 163–190.

Haëntjens, N., Boss, E., Talley, L.D., 2017. Revisiting Ocean Color algorithms for chlorophyll a and particulate organic carbon in the S outhern Ocean using biogeochemical floats. J. Geophys. Res. Oceans 122, 6583–6593.

Haynes, J.M., Jakob, C., Rossow, W.B., Tselioudis, G., Brown, J., 2011. Major characteristics of Southern Ocean cloud regimes and their effects on the energy budget. J. Clim. 24, 5061–5080.

He, X., Stamnes, K., Bai, Y., Li, W., Wang, D., 2018. Effects of Earth curvature on atmospheric correction for ocean color remote sensing. Remote Sens. Environ. 209, 118–133.

Holm-Hansen, O., Kahru, M., Hewes, C., Kawaguchi, S., Kameda, T., Sushin, V., Krasovski, I., Priddle, J., Korb, R., Hewitt, R., 2004. Temporal and spatial distribution of chlorophyll-a in surface waters of the Scotia Sea as determined by both shipboard measurements and satellite data. Deep Sea Res. Part II 51, 1323–1331.

Holm-Hansen, O., Lorenzen, C.J., Holmes, R.W., Strickland, J.D., 1965. Fluorometric determination of chlorophyll. ICES J. Mar. Sci. 30, 3–15.

Hooker, S.B., Morel, A., 2003. Platform and environmental effects on above-water determinations of water-leaving radiances. Journal of Atmospheric Oceanic Technology 20, 187–205.

Hu, C., Feng, L., Lee, Z., Franz, B.A., Bailey, S.W., Werdell, P.J., Proctor, C.W., 2019. Improving satellite global chlorophyll a data products through algorithm refinement and data recovery. J. Geophys. Res. Oceans 124, 1524–1543.

Hu, C., Lee, Z., Franz, B., 2012. Chlorophyll a algorithms for oligotrophic oceans: a novel approach based on three-band reflectance difference. J. Geophys. Res. Oceans 117.

IOCCG, 2015. Ocean Colour Remote Sensing in Polar Seas: Report of an IOCCG Working Group on Ocean Colour Remote Sensing in Polar Seas. In: Babin, M., Arrigo, K.R., Bélanger, S., Forget, M.-.-H. (Eds.), *IOCCG Report Series*. Dartmouth, NS, Canada, International Ocean Colour Coordinating Group.

Jena, B., 2017. The effect of phytoplankton pigment composition and packaging on the retrieval of chlorophyll-a concentration from satellite observations in the Southern Ocean. Int. J. Remote Sens. 38, 3763–3784.

Johnson, R., Strutton, P.G., Wright, S.W., McMinn, A., Meiners, K.M., 2013. Three improved satellite chlorophyll algorithms for the Southern Ocean. J. Geophys. Res. Oceans 118, 3694–3703.

Kostadinov, T., Siegel, D., Maritorena, S., 2009. Retrieval of the particle size distribution from satellite ocean color observations. J. Geophys. Res. Oceans 114.

Lee, Z., Ahn, Y.-H., Mobley, C., Arnone, R., 2010. Removal of surface-reflected light for the measurement of remote-sensing reflectance from an above-surface platform. Opt. Express 18, 26313–26324.

Lee, Z., Wang, T., Zhao, L., Wang, D., Ye, X., Shang, S., Yu, X., 2024. Cross-satellite atmospheric correction for consistent remote sensing reflectance from multiple ocean color satellites: Concept and demonstrations. Journal of Remote Sensing 4, 0302.

Li, H., He, X., Bai, Y., Chen, X., Gong, F., Zhu, Q., Hu, Z., 2017. Assessment of satellite-based chlorophyll-a retrieval algorithms for high solar zenith angle conditions. J. Appl. Remote Sens. 11, 012004.

Li, H., He, X., Bai, Y., Gong, F., Wang, D., Li, T., 2022. Restoration of wintertime ocean color remote sensing products for the high-latitude oceans of the Southern Hemisphere. IEEE Transactions on Geoscience Remote Sensing 60, 1–12.

Li, J., Antoine, D., Huot, Y., 2024. Bio-optical variability of particulate matter in the southern ocean. Front. Mar. Sci. 11, 1466037.

Long, M.C., Stephens, B.B., McKain, K., Sweeney, C., Keeling, R.F., Kort, E.A., Morgan, E. J., Bent, J.D., Chandra, N., Chevallier, F., 2021. Strong Southern Ocean carbon uptake evident in airborne observations. Science 374, 1275–1280.

Marrari, M., Hu, C., Daly, K., 2006. Validation of SeaWiFS chlorophyll a concentrations in the Southern Ocean: a revisit. Remote Sens. Environ. 105, 367–375.

Mayewski, P.A., Meredith, M., Summerhayes, C., Turner, J., Worby, A., Barrett, P., Casassa, G., Bertler, N.A., Bracegirdle, T., Naveira Garabato, A., 2009. State of the Antarctic and Southern Ocean climate system. Rev. Geophys. 47.

Mobley, C.D., 1999. Estimation of the remote-sensing reflectance from above-surface measurements. Appl. Opt. 38, 7442–7455.

Moore, J.K., Abbott, M.R., Richman, J.G., Smith, W.O., Cowles, T.J., Coale, K.H., Gardner, W.D., Barber, R.T., 1999. SeaWiFS satellite ocean color data from the Southern Ocean. Geophys. Res. Lett. 26, 1465–1468.

Morel, A., Prieur, L., 1977. Analysis of variations in ocean color 1. Limnol. Oceanogr. 22, 709–722.

Morley, S.A., Abele, D., Barnes, D.K., Cárdenas, C.A., Cotté, C., Gutt, J., Henley, S.F., Höfer, J., Hughes, K.A., Martin, S.M., 2020. Global drivers on southern ocean ecosystems: changing physical environments and anthropogenic pressures in an earth system. Front. Mar. Sci. 7, 547188.

Moutier, W., Thomalla, S.J., Bernard, S., Wind, G., Ryan-Keogh, T.J., Smith, M.E., 2019. Evaluation of chlorophyll-a and POC MODIS aqua products in the southern ocean. Remote Sens. (Basel) 11, 1793.

Murphy, E.J., Johnston, N.M., Hofmann, E.E., Phillips, R.A., Jackson, J.A., Constable, A. J., Henley, S.F., Melbourne-Thomas, J., Trebilco, R., Cavanagh, R.D., 2021. Global connectivity of Southern Ocean ecosystems. Frontiers in Ecology Evolution 9, 624451.

O'Reilly, J.E., Maritorena, S., Mitchell, B.G., Siegel, D.A., Carder, K.L., Garver, S.A., Kahru, M., McClain, C., 1998. Ocean color chlorophyll algorithms for SeaWiFS. J. Geophys. Res. Oceans 103, 24937–24953.

O'Reilly, J.E., Werdell, P.J., 2019. Chlorophyll algorithms for ocean color sensors-OC4, OC5 & OC6. Remote Sens. Environ. 229, 32–47.

O'Reilly, J.E.M., S.; O'Brien, M.C.; Siegel, D.A.; Toole, D.; Menzies, D.; Smith, R.C.; Mueller, J.L.; Mitchell, B.G.; Kahru, M.; Chavez, F.P.; Strutton, P.; Cota, G.F.; Hooker, S.B.; McClain, C.R.; Carder, K.L.; Muller-Karger, F.; Harding, L.; Magnuson, A.; Phinney, D.; Moore, G.F.; Aiken, J.; Arrigo, K.R.; Letelier, R.; Culver, M. (2000). SeaWiFS postlaunch calibration and validation analyses, part 3. In, *SeaWiFS Postlaunch Technical Report Series* (pp. 1–49). Greenbelt, MD: NASA Center for AeroSpace Information.

Randolph, K., Dierssen, H.M., Cifuentes-Lorenzen, A., Balch, W.M., Monahan, E.C., Zappa, C.J., Drapeau, D.T., Bowler, B.J.J.o.A., & Technology, O. (2017). Novel methods for optically measuring whitecaps under natural wave-breaking conditions in the Southern Ocean. *Journal of Atmospheric and Oceanic Technology, 34*, 533-554.

Robinson, C.M., Huot, Y., Schuback, N., Ryan-Keogh, T.J., Thomalla, S.J., Antoine, D., 2021. High latitude Southern Ocean phytoplankton have distinctive bio-optical properties. Opt. Express 29, 21084–21112.

Ruddick, K.G., Ovidio, F., Rijkeboer, M., 2000. Atmospheric correction of SeaWiFS imagery for turbid coastal and inland waters. Appl. Opt. 39, 897–912.

Salyuk, P.A., Glukhovets, D.I., Latushkin, A.A., Kalinina, O.Y., Shtraikhert, E.A., Sapozhnikov, P.V., Mosharov, S.A., Stepochkin, I.E., Lipinskaya, N.A., Gorbov, M.I., 2025. Extreme underestimation of satellite-derived chlorophyll-a concentration in the northwestern Weddell Sea during a phytoplankton bloom and its reasons. J. Mar. Syst. 104159.

Scanlon, B., Ward, B., 2016. The influence of environmental parameters on active and maturing oceanic whitecaps. J. Geophys. Res. Oceans 121, 3325–3336.

Simmonds, I., 2003. Modes of atmospheric variability over the Southern Ocean. J. Geophys. Res. Oceans 108.

Song, C., Ke, L., 2015. Bathymetrical influences on spatial and temporal characteristics of chlorophyll-a concentrations in the Southern Ocean from 2002 to 2012 (October to March) using MODIS. Geo-spatial Inf. Sci. 18, 200–211.

Thomalla, S.J., Nicholson, S.-A., Ryan-Keogh, T.J., Smith, M.E., 2023. Widespread changes in Southern Ocean phytoplankton blooms linked to climate drivers. Nat. Clim. Chang. 13, 975–984.

Tripathy, S., Pavithran, S., Sabu, P., Naik, R., Noronha, S., Bhaskar, P., & Anilkumar, N. (2014). Is primary productivity in the Indian Ocean sector of Southern Ocean affected by pigment packaging effect? *current science*, 1019-1026.

Wang, M., 2002. The Rayleigh lookup tables for the SeaWiFS data processing: Accounting for the effects of ocean surface roughness. Int. J. Remote Sens. 23, 2693–2702.

Wang, T., Lee, Z., Li, X., Zhao, L., Yu, X., Wang, D., Shang, S., 2026. Improving the accuracy and spatial coverage of remote sensing reflectance from VIIRS under strong sunglint and high solar zenith angle via cross-satellite atmospheric correction. IEEE Trans. Geosci. Remote Sens.

Wei, J., Lee, Z., Shang, S., 2016. A system to measure the data quality of spectral remote-sensing reflectance of aquatic environments. J. Geophys. Res. Oceans 121, 8189–8207.

Welschmeyer, N.A., 1994. Fluorometric analysis of chlorophyll a in the presence of chlorophyll b and pheopigments. Limnol. Oceanogr. 39, 1985–1992.

Williams, R.G., Ceppi, P., Roussenov, V., Katavouta, A., Meijers, A.J., 2023. The role of the Southern Ocean in the global climate response to carbon emissions. Phil. Trans. R. Soc. A 381, 20220062.

Zhang, Y., Yu, X., Lee, Z., Shang, S., Qiao, H., Lin, G., Lai, W., 2024. Performance of two semi-analytical algorithms in deriving water inherent optical properties in the Southern Ocean. Opt. Express 32, 15741–15759.